Laser-Accelerated, Low-Divergence 15-MeV Quasimonoenergetic Electron Bunches at 1 kHz

F. Salehi,[1] M. Le,[1] L. Railing,[1] M. Kolesik,[2] and H. M. Milchberg[1,*]

[1]*Institute for Research in Electronics and Applied Physics, University of Maryland, College Park, Maryland 20742, USA*

[2]*College of Optical Sciences, University of Arizona, Tucson, Arizona 85712, USA*

(Received 29 October 2020; revised 1 February 2021; accepted 20 April 2021; published 11 June 2021)

We demonstrate laser wakefield acceleration of quasimonoenergetic electron bunches up to 15 MeV at 1-kHz repetition rate with 2.5-pC charge per bunch and a core with <7-mrad beam divergence. Acceleration is driven by 5-fs, <2.7-mJ laser incident on a thin, near-critical-density hydrogen gas jet. Low beam divergence is attributed to reduced sensitivity to laser carrier-envelope phase slip, achieved in two ways using gas jet positon control and laser polarization: (i) electron injection into the wake on the gas jet's plasma density downramp and (ii) use of circularly polarized drive pulses. These results demonstrate the generation of high-quality electron beams from a few-cycle-pulse-driven laser plasma accelerator without the need for carrier-envelope phase stabilization.

DOI: 10.1103/PhysRevX.11.021055

Subject Areas: Atomic and Molecular Physics, Optics, Plasma Physics

I. INTRODUCTION

There is a large demand for high-energy electron beams with a wide range of parameters for various applications in science, industry, and medicine [1,2]. Laser wakefield acceleration (LWFA) in plasmas [3,4] could potentially replace conventional accelerators for some of these tasks and open up new applications due to their compact footprint and bright, ultrashort bunches [5]. In the past two decades, advances in peak laser power [6], along with new laser plasma interaction targets [7], have led to the evolution of accelerated electron bunches from wide-divergence, tens-of-MeV thermal spectrum beams [8,9] to ∼100-MeV quasimonoenergetic low-divergence beams [10–12] and, most recently, quasimonoenergetic bunches up to 8 GeV [13]. The goal of many recent experiments [7,14–16] is multi-GeV electron bunch energies in a single acceleration stage; this requires low plasma densities ($N_e/N_{cr} < \sim 10^{-3}$, where N_{cr} is the critical plasma density) to mitigate dephasing, and high laser pulse energy of at least several joules. Consequently, such experiments are limited to a low repetition rate (≤10 Hz) with current laser technology.

For many applications, electron bunch energy in the approximately ∼1–20 MeV range is of interest, where the main challenges are increasing the repetition rate and the bunch charge and improving the energy spread, emittance, and laser-to-electron energy conversion efficiency. Early, low-repetition-rate LWFA experiments applied few-MeV thermal bunches or their bremsstrahlung gamma rays to radiography [17–20]. More recent kilohertz-repetition-rate LWFA experiments have used the generated ∼100-keV beams for electron diffraction [21], and there are proposals to use kHz LWFA sources for electron diffraction at MeV energies [22]. A high-repetition-rate quasimonoenergetic multi-MeV electron beam source would benefit all such applications while enabling improved data statistics.

In recent years, multiple groups have generated kilohertz-repetition-rate electron bunches using various laser interaction targets. The use of liquid or solid targets has led to large divergence <3-MeV thermal beams which counterpropagate with respect to the incident laser pulse [23,24]. In experiments using subcritical-density gas targets, focusing 10-mJ laser pulses on the density downramp of an argon or helium jet led to ∼100-keV, 10-fC electron bunches [25]. The use of near-critical hydrogen and helium jets by our group enabled relativistic self-focusing of 10-mJ-scale laser pulses and led to the first demonstration of >MeV bunches from gas targets at a kilohertz repetition rate [26]. However, because our laser pulse width was several times the plasma period, these electrons were accelerated in the self-modulated laser wakefield (SM-LWFA) regime, giving a large thermal energy spread with a wide FWHM beam divergence $\theta_{div} \sim 200$ mrad. More recently, the first kilohertz-repetition-rate experiments to use few-cycle drive pulses ($f/2$ focusing of 3.4-fs, <2.5-mJ pulses onto a high-density nitrogen gas jet) have led to the acceleration of quasimonoenergetic <5-MeV,

*milch@umd.edu

$\theta_{\mathrm{div}} \sim 45$ mrad bunches, with electron injection from ionization of He-like nitrogen (N^{5+}) [27–29].

In this paper, we describe experiments in which we generate up to 15-MeV quasimonoenergetic low-divergence electron bunches using few-cycle, low-energy ($\tau \sim 5$ fs FWHM, 2.2–2.7 mJ) laser pulses interacting with near-critical-density hydrogen jet targets in the bubble (or blowout) [30,31] regime. Control of the laser's polarization and focal position in the gas jet can tune the electron beam's energy, divergence, and transverse profile. Under optimized conditions using circularly polarized drive pulses, we obtain quasimonoenergetic electron beams with energy $E_b \sim 15$ MeV and $\Delta\theta_{\mathrm{div}} < 7$ mrad FWHM divergence. Crucial to achieving high energy and low divergence are a longer laser-focusing geometry enabled by reduced ionization-induced refraction by the H_2 gas target and use of circular polarization, which strongly mitigates the deleterious effects of the few-cycle drive pulse's carrier-envelope phase (CEP) slip on the bubble dynamics and accelerating field.

II. EXPERIMENTAL SETUP

The few-cycle, non-CEP-stabilized, LWFA drive pulse is generated by guiding and self-phase modulation (SPM) of a 35-fs FWHM, <6-mJ, $\lambda = 800$ nm Ti:sapphire laser pulse in a 2.5-m-long, 500-μm-inner-diameter hollow core fiber (HCF) with helium gas injected near the fiber exit and pumped out near the entrance [32]. See Fig. 1(a). Before injection into the HCF, the pulse polarization is adjusted by a quarter wave plate where, depending on the input ellipticity, the HCF exit spectrum [Fig. 1(b)] can reach ~200 nm FWHM with a central wavelength $\lambda_0 \sim 650$ nm. After propagation through a chirped mirror compressor (90% throughput) and a pair of wedges for fine-tuning the pulse length [48], the beam is directed into the experimental chamber. The pulse loses more than half of its energy through leakage from the HCF and losses from the compressor, beam routing mirrors, and windows. Ultimately, 2.2–2.7 mJ in a 5-fs FWHM pulse [49] is focused by an $f/6.5$ off-axis paraboloid to a 4.5-μm FWHM intensity spot, giving a confocal parameter $2z_0 \sim 100$ μm and a peak vacuum intensity 2.3×10^{18} W/cm^2 (peak normalized vector potential $a_0 = 0.9$). A reflection at the wedges is used as a probe for interferometry and

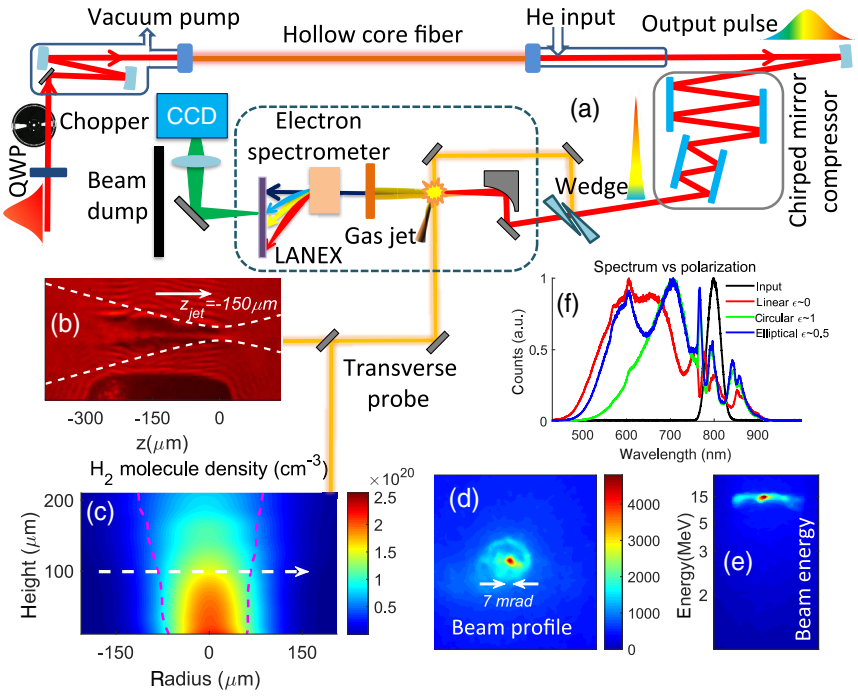

FIG. 1. Experimental setup. (a) Laser pulses with few-cycle duration, generated through a hollow core fiber (HCF) and a chirped mirror compressor, are used to drive electron acceleration from a near-critical-density hydrogen jet target. A probe pulse split from the main drive pulse is used for (b) probing of the few-cycle pulse interaction with the jet and (c) interferometric measurement of the jet density. The white arrows show the drive beam propagation direction, the white dashed lines [(b)] indicate the laser beam $4e^{-2}$ Gaussian intensity envelope, and the red dashed lines [(c)] show the density FWHM contour. (d),(e) Sample electron beam profile and energy spectrum as imaged on the LANEX screen. (f) HCF output spectrum as a function of input polarization (input energy 6 mJ). Elliptical input polarization ($\varepsilon = 0.5$) generates the broadest output spectrum, which is near-circularly polarized. LP beams are polarized left-right in electron beam profile and spectrum images such as (d) and (e).

shadowgraphy of the gas jet target and the laser-target interaction.

The near-critical-density jet is produced by feeding high-pressure hydrogen gas through a solenoid valve to a Mach 2.9 supersonic nozzle with a 100-μm-diameter throat. The near-Gaussian gas density profile, measured with the probe pulse, is shown in Fig. 1(c). In the laser beam path $\sim$100 μm above the nozzle orifice, the jet is $\sim$150 μm FWHM with a peak H_2 density adjusted in the range $N_m = 1.0\text{–}1.7 \times 10^{20}$ cm^{-3}. When fully ionized, this yields electron density in the range $N_e/N_{\rm cr} = 0.08\text{–}0.13(\pm \sim 15\%)$, where $N_{\rm cr} = 2.64 \times 10^{21}$ cm^{-3} is the critical plasma density at $\lambda_0 = 650$ nm. Earlier versions of this gas jet [50] were used to generate near-critical-density targets for experiments in the SM-LWFA regime [26,51,52]. For the conditions of this experiment, we observe electron beams only from hydrogen jets. No comparable electron beams are observed using other gases (He, N_2, and Ar), for which our particle-in-cell (PIC) simulations [32] and interferometric images show that ionization-induced defocusing refracts and distorts the pulse before the onset of relativistic self-focusing. Tighter focusing at $f/3.2$ partially mitigates ionization defocusing but leads to electron beams with lower energy and higher divergence [49]. Here, the 10^{14} W/cm^2 ionization threshold of hydrogen leads to saturated ionization of the target well into the transverse wings of the pulse's leading edge, mitigating ionization-induced refraction and enabling the use of longer $f/6.5$ focusing, promoting greater acceleration in the longer laser-plasma interaction length.

For electron energy spectrum measurements, three different sets of permanent magnet dipoles with magnetic field $0.08T\text{–}0.35T$ were used between the jet and a LANEX fluorescing screen (located 30 cm beyond the jet), which was imaged by a low-noise CCD camera. Full electron beam profiles were measured by translating the magnet out of the beam path. Figure 1 shows the magnetic spectrometer [Fig. 1(a)] and examples of an electron beam profile and energy spectrum [Figs. 1(d) and 1(e), respectively].

The radiation dose from the electron beam measured in the forward direction, from bremsstrahlung conversion in the aluminum and lead beam dump, was >1 μrad per shot for the highest-energy electron bunches ($E_b \sim 15$ MeV) measured in the experiment. To avoid high dose accumulation at the kilohertz pulse repetition rate of the laser, we opened the gas jet's solenoid valve for a 10-ms interval every 2 s. In addition, when generating >10-MeV electron bunches, we used a chopper in the laser beam path to lower the pulse repetition rate to 100 Hz. The accelerator average repetition rate to was thus lowered to 0.5 Hz, reducing the accumulated dose by 2000×. To assess the effect of continuous operation at 1 kHz, we opened the valve for 1-s intervals, during which the chamber background pressure rose from 20 to 150 mTorr. To keep radiation low, ten shot bursts were collected every 0.1 s over this interval, over which the electron beam profile shape, pointing, divergence, and quasimonoenergetic energy spectrum remained consistent, with the main effect being a $\sim$60% reduction in charge per shot after 0.5 s, after which it stabilized. This result is consistent with our prior high-repetition-rate results in the SM-LWFA regime [26], where the main effect of increasing background pressure (up to 20 Torr) was bunch charge reduction.

The maximum pulse energy injected into the HCF is limited by the critical self-focusing power and the ionization threshold of the gas flowing in the fiber, here helium. Excessive ionization of He leads to significant blueshifting of the spectrum [53], increased coupling and guiding losses, and deterioration of the spectral phase, making compression to few-cycle pulse widths difficult. The highest input pulse energy is set near the threshold at which filamentation in He is observed at the fiber entrance. Circularly polarized (CP) pulses have a higher tunneling ionization threshold than linear polarized (LP) pulses, so it is typical to inject gas-filled hollow core fibers with higher-energy CP pulses, generate a SPM-broadened spectrum, and then convert the fiber output back to LP [48,54]. In our experiment, we observe that the use of elliptically polarized input pulses leads to larger bandwidth and, in turn, shorter compressed pulses than with LP or CP input pulses, where partial He ionization at the onset of filamentation plays a role [55]. Figure 1(f) shows fiber exit spectra for a 6-mJ input pulse for a range of input polarization ellipticities ϵ, the ratio of minimum to maximum electric field in the polarization ellipse. The largest output bandwidth occurs for $\epsilon \sim 0.5$, where the output pulse has a double-hump spectrum with $\sim$200 nm bandwidth. In this case, the ellipticity evolves during the pulse propagation in the fiber [56], and we measure nearly CP output pulses, $\epsilon \sim 0.9$. Here, the shortest pulse duration after compression is 5 fs. For CP input pulses, the comparatively smaller exit bandwidth precludes compression below $\sim$7 fs, and no significant electron acceleration is observed with those beams. The Supplemental Material [32] shows simulations of elliptically polarized input pulses evolving to near-CP output pulses.

III. RESULTS AND DISCUSSION

We first examine the effect of laser focusing on electron beam divergence. Here, the laser energy and plasma density were both chosen to be on the low end of our parameter range to promote self-focusing and wake generation on the laser pulse exit side (downramp density side) of the hydrogen jet. Figure 2(a) shows profiles of accelerated electron bunches as a function of the jet center position $z = z_{\rm jet}$ with respect to the laser focus ($z = 0$). Here, we used 2.2-mJ, 5-fs LP drive pulses, with a peak electron density at jet center of $N_{e,\rm peak}/N_{\rm cr} = 0.08$, giving $(P/P_{\rm cr})_{\rm max} \sim 2$ for these conditions, where the minimum

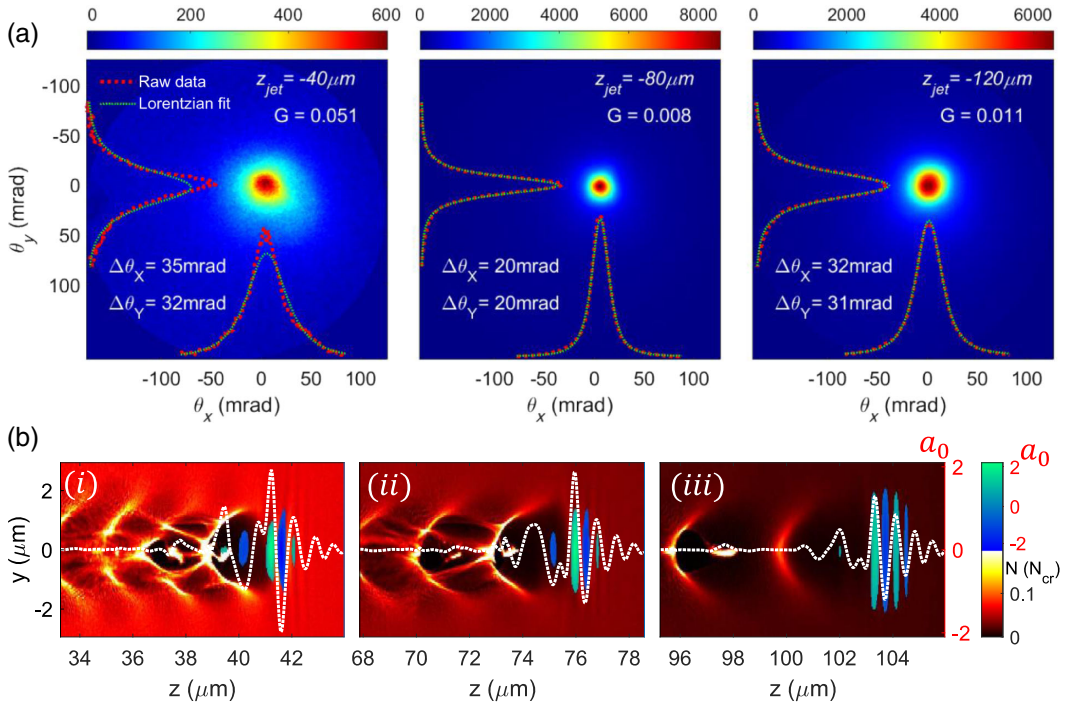

FIG. 2. Experimental conditions: 2.2-mJ, 5-fs LP drive pulse, peak jet plasma density $N_{e,\mathrm{peak}}/N_{\mathrm{cr}} = 0.08$, $(P/P_{\mathrm{cr}})_{\mathrm{max}} \sim 2$. (a) Electron beam profiles, θ_x and θ_y lineouts, and Lorentzian fits for varying position of the jet center (z_{jet}) relative to the laser beam waist at $z = 0$ (ten-shot burst). The Lorentzian fit quality is reduced as the jet center moves closer to the beam waist, with rms fit error G [32] shown in each panel. (b) PIC simulations [32], showing normalized laser vector potential a (color map and dashed white line) overlaid on electron density. To illustrate plasma wave injection at locations progressively farther into the density downramp, laser propagation is launched at beam waists located (i) 10 μm past the jet center, (ii) 30 μm past the jet center, and (iii) 50 μm past the jet center. The horizontal scale is distance from the jet center. Simulation parameters: $a_0 = 1$, 5-fs LP drive pulse, peak plasma density $N_{e,\mathrm{peak}}/N_{\mathrm{cr}} = 0.08$, and jet FWHM 140 μm.

critical power for relativistic self-focusing is $P_{\mathrm{cr,min}} = 17.4(N_{\mathrm{cr}}/N_{e,\mathrm{peak}})$ GW [57]. Images represent the average of ten successive ten-shot bursts collected during a 10-ms valve-opening time; these ten-shot bursts were quite stable, with burst-to-burst pointing jitter as small as 2 mrad. Starting at $z_{\mathrm{jet}} = -200$ μm (vacuum focus 200 μm beyond the jet center), we observed a barely detectable electron beam (~10 fC) with a large divergence angle ($\Delta\theta_{\mathrm{div}} > 50$ mrad) and low energy ($E_b \gtrsim 0.2$ MeV). Moving the jet forward toward the focus, $\Delta\theta_{\mathrm{div}}$ continuously decreases to a minimum of 20 mrad [Fig. 2(a), $z_{\mathrm{jet}} = -80$ μm], where the laser waist is located near the jet's far side half-maximum density, generating ~2-pC, ~0.5-MeV quasimonoenergetic (QME) beams. Moving the jet center closer to the beam waist, the divergence increases again to $\Delta\theta_{\mathrm{div}} \sim 34$ mrad [Fig. 2(a), $z_{\mathrm{jet}} = -40$ μm]. As the jet is moved to the beam waist at $z_{\mathrm{jet}} = 0$, $\Delta\theta_{\mathrm{div}}$ and E_b continuously increase to >70−mrad and ~3-MeV QME beams, but the total charge per shot drops and the beam disappears as the jet center is moved past the beam waist ($z_{\mathrm{jet}} = +20$ μm).

The simulations in Fig. 2(b) qualitatively explain the trends as follows: When electron injection occurs in the density downramp [58,59] (the half-peak density is at $z = 70$ μm), the laser spot w_l matches the bubble radius, $w_l \sim R_b = 2k_p^{-1}\sqrt{a} \sim 1.4$ μm [31], where k_p is the plasma wave number and $a \sim 1.8$ is the peak normalized laser vector potential in the plasma. Here, the expansion of the bunch in the downramp reduces its divergence [60,61] [(ii)]. Further in the downramp [(iii)], injection occurs only in the lower phase velocity second plasma wave bucket, where the defocusing force behind the first bucket imposes a larger beam divergence. Closer to the jet density peak, self-injection from wave breaking becomes important [(i)], which degrades bunch divergence.

The electron beam profiles shown in Fig. 2(a) are an excellent fit to the 2D Lorentzian profile $\sigma_q \propto \{1+[(x-x_0)/w_x]^2 + [(y-y_0)/w_y]^2\}^{-1.5}$, where $\sigma_q(x,y)$ is the charge density on the screen,(x_0, y_0) is the profile center, and w_x and w_y are the charge spread in each dimension. For the images shown here, LANEX screen fluorescence is linear in the local beam flux [32]. The goodness of fit is quantified by the normalized rms error G [32] indicated in Fig. 2(a), where it is seen that G deteriorates as the beam waist moves closer to the jet center or past the midrange of the downramp. We observe the Lorentzian charge density

profile for almost any pulse energy and plasma density if the jet center is located far enough upstream of the vacuum focus. For the small transverse bunch size at the plasma exit (~1–2 μm), the transverse momentum distribution is imprinted onto the beam spatial profile at the screen according to $x/L \sim \Delta p_x/p_\parallel$ and $y/L \sim \Delta p_y/p_\parallel$, where L is the gas jet−screen distance. A Lorentzian beam profile can be explained as the composition of several Gaussian-distributed (in $\Delta p_\perp/p_\parallel$) electron populations of varying divergence. This explanation might be expected from bunches accelerated by multiple plasma wave buckets. Alternatively, we note that the electron bunches generated by few-cycle pulses in near-critical plasma are strongly correlated collisionless plasmas far from equilibrium and may follow a so-called κ ("kappa") momentum distribution that would spatially imprint on the detector screen as a Lorentzian profile [32].

For the short gas jet used in these experiments, higher-energy electron beams require higher-energy laser pulses driving higher-density plasma [consistent with the LWFA nonlinear dephasing length [31] near peak density (here $< \sim 50$ μm)]. Figure 3 shows the electron bunch profile and energy spectrum for higher-energy LP drive pulses (2.6 mJ) and higher peak plasma density ($N_{e,\mathrm{peak}}/N_{\mathrm{cr}} \sim 0.12$), giving $(P/P_{\mathrm{cr}})_{\mathrm{max}} \sim 3.5$, where we compare results for the vacuum beam waist positioned near the jet center ($z_{\mathrm{jet}} = 20$ μm) and in the density downramp ($z_{\mathrm{jet}} = -110$ μm). As in the experiments in Fig. 2, the electron bunch energy and divergence increase for the vacuum beam waist near the jet center (here, $E_b \sim 9$ MeV, $\Delta\theta_{\mathrm{div}} \sim 300$ mrad, and charge ~1.7 pC) with the energy dropping for the beam waist on either side of it. Here, simulations show that the beam's wide divergence and non-Lorentzian profile ($G = 0.14$) result from self-injection via catastrophic wave breaking. The best pointing stability and lowest divergence occur for the beam waist in the density downramp, where, for $z_{\mathrm{jet}} = -110$ μm, we measure $E_b \sim 3$ MeV, $\Delta\theta_{\mathrm{div}} \sim$ 45 mrad, and accelerated charge of ~2.2 pC per shot. Here, the beam profile is better fit by a Lorentzian ($G = 0.05$), but $\Delta\theta_{\mathrm{div}}$ is larger than in Fig. 2's case of low pulse energy and low plasma density.

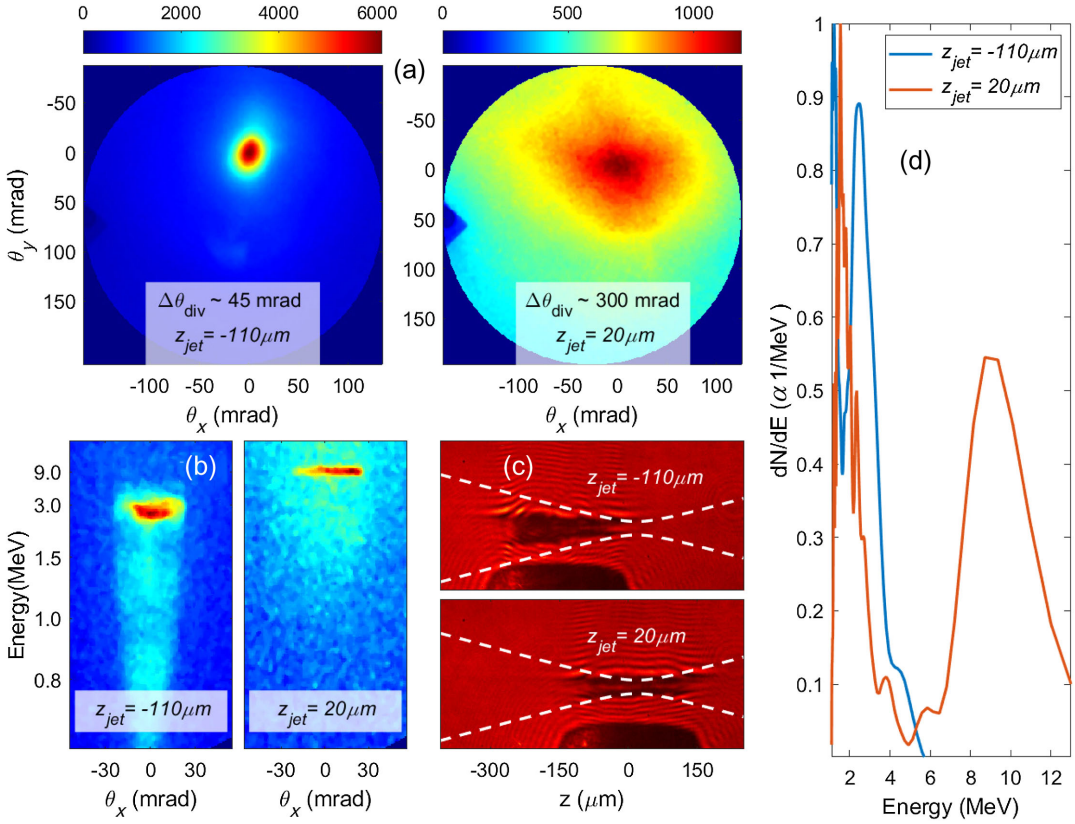

FIG. 3. Experimental conditions: 2.6-mJ, 5-fs LP drive pulse, peak jet plasma density $N_{e,\mathrm{peak}}/N_{\mathrm{cr}} = 0.12$, $(P/P_{\mathrm{cr}})_{\mathrm{max}} \sim 3.5$. (a) Electron beam profiles for the vacuum beam waist near the jet center ($z_{\mathrm{jet}} = 20$ μm) and in the density downramp ($z_{\mathrm{jet}} = -110$ μm). (b) Corresponding electron bunch spectra and (c) shadowgraphic images, which show the beam focus near the jet center (bottom) and in the downramp (top). The dashed white lines show the $4e^{-2}$ envelope of the vacuum beam. (d) Lineouts of angle-integrated electron spectra of (b) on a linear energy scale. The resolution of the QME peaks is reduced by some penetration of high-energy electrons through the spectrometer slit edges. The electron beam profiles and spectra are averages from ten-shot bursts.

The results presented so far indicate that, for LWFA driven by few-cycle laser pulses in near-critical plasma, the price paid for high-energy electron bunches is larger beam divergence. One potential source of divergence associated with few-cycle drivers is presented in prior simulations [62,63]: the CEP slip caused by the difference in the pulse's phase and group velocities in plasma. This difference increases with plasma density and is significant in our experiments. For a LP driver, CEP slip has the effect of driving a transverse oscillation in the wake bubble along the laser polarization direction, resulting in an asymmetric acceleration field experienced by the electron bunch. This effect suggests that a possible way to promote greater symmetry is to use a CP driver pulse.

In Fig. 4, we show the result of using a CP 5-fs drive pulse, for laser energy 2.7 mJ, $N_{e,\mathrm{peak}}/N_{\mathrm{cr}} = 0.10$, and $(P/P_{\mathrm{cr}})_{\mathrm{max}} \sim 3.1$. As in the prior figures, we compare acceleration for varying vacuum beam waist position with respect to the jet center. Starting with the jet center far upstream of the focus, $z_{\mathrm{jet}} = -130\ \mu$m (or focus in the

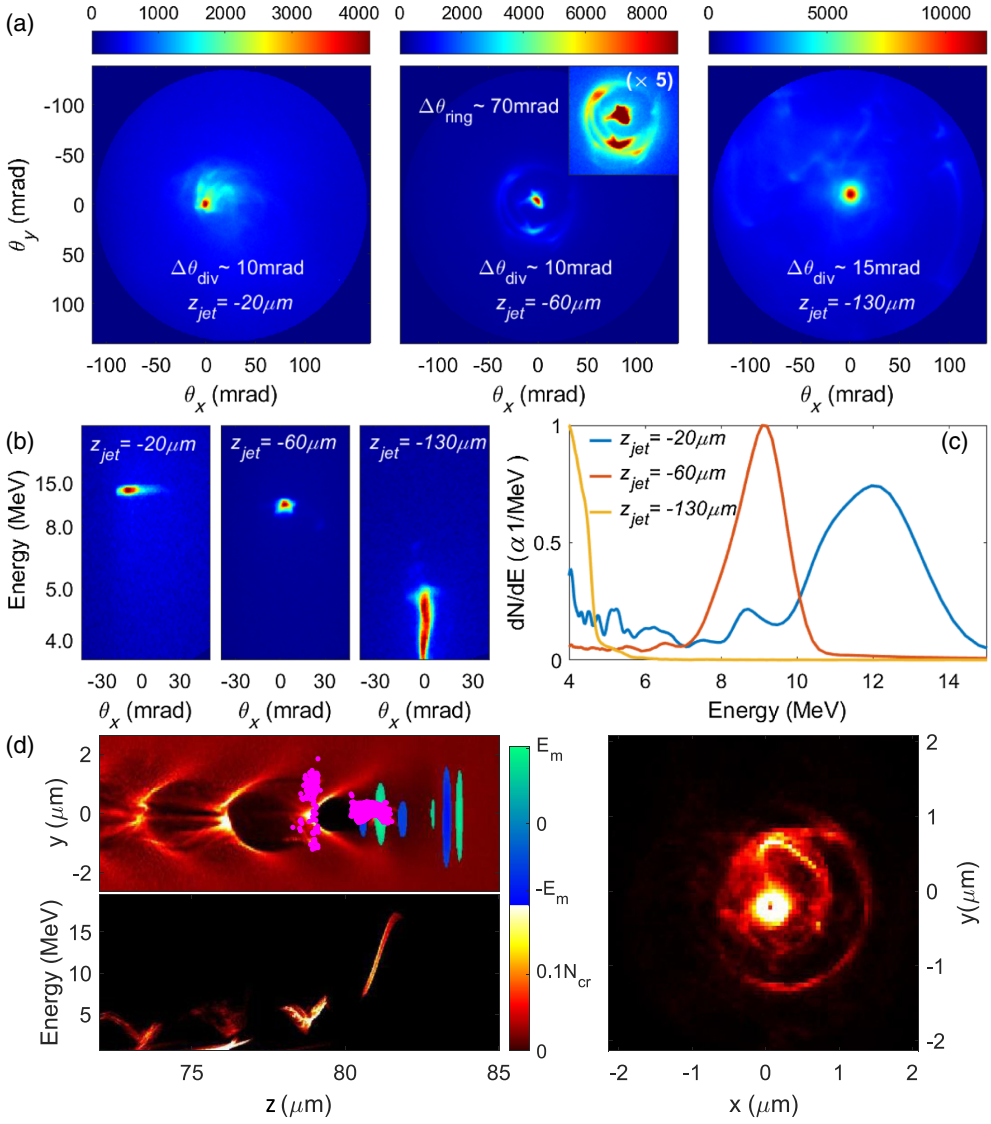

FIG. 4. Experimental conditions: 2.7-mJ, 5-fs CP drive pulse, peak jet plasma density $N_{e,\mathrm{peak}}/N_{\mathrm{cr}} = 0.10$, $(P/P_{\mathrm{cr}})_{\mathrm{max}} \sim 3.1$. (a) Single-shot electron beam profiles for varying z_{jet}. The middle panel inset for $z_{\mathrm{jet}} = -60\ \mu$m (near half-peak density in the downramp) shows the electron ring image enhanced by 5×. (b) Corresponding energy spectra. (c) Energy spectra lineouts plotted on a linear scale. (d) PIC simulation result for a CP pulse with injection near half-maximum density in the downramp. Electrons (magenta dots) injected in the second bucket form a ring in the transverse plane (right) as they outrun the first bucket. The electrons in the ring have a lower energy than those in the central spot (bottom left). Simulation parameters: pulse energy 2.7 mJ, pulse width 5 fs, vacuum spot FWHM 4.5 μm, jet FWHM 140 μm, $z_{\mathrm{jet}} = -60\ \mu$m, and $N_e/N_{\mathrm{cr}} = 0.1$.

downramp), the beam has a 2D Lorentzian shape ($G = 0.03$), with a divergence significantly reduced to $\Delta\theta_{\rm div} \sim 15$ mrad, approximately 3× smaller than the LP case. The bunch charge is ∼9 pC and $E_b \lesssim 5$ MeV in a non-QME spectrum. For $z_{\rm jet} = -60$ μm, the ∼3-pC beam has a tight central spot ($\Delta\theta_{\rm div} \sim 10$ mrad) with a 9-MeV QME peak with $\Delta E_b/E_b \sim 0.2$, surrounded by a lower-energy ring structure with a full width divergence of ∼70 mrad. The beam image is shown enhanced by 5× in the inset.

The ring structure appears only with the CP driver. Moving the laser beam waist further toward the jet center, $z_{\rm jet} = -20$ μm, the ring transforms into a ∼50-mrad pedestal surrounding a central spot with $\Delta\theta_{\rm div} \sim 10$ mrad. Here, the bunch has a ∼12-MeV QME peak with $\Delta E_b/E_b \sim 0.25$ and a total charge of ∼3.5 pC. The divergence of the central peak is approximately 30× smaller than in the LP case.

We attribute this dramatic reduction in electron beam divergence for a CP driver to reduced laser-induced distortion of the first LWFA bucket (bubble) following the laser pulse. As mentioned, prior simulations [62,63] show that a few-cycle LP driver pulse oscillates the bubble along the laser polarization direction, distorting the bubble's accelerating field and the accelerated bunch. This effect is quite different from the case of hosing instability with many-cycle pulses, where the ponderomotive potential driving the wakefield is similar for LP and CP pulses. The few-cycle effect is enhanced by the large laser redshift and the plasma's negative group velocity dispersion, which causes the laser field to slip to the back of the first bucket and even into the second bucket.

To visualize the effects of a few-cycle driver on the bubble and its accelerating field, Fig. 5 shows the results of simulations contrasting LP and CP pulse interaction with a neutral H_2 jet, with the beam waist at the jet center, and using our experimental parameters (see the figure caption). Figure 5(a) plots the time evolution of the normalized bubble centroid position $(\bar{x}/R_b, \bar{y}/R_b)$ in the transverse plane. Here, $(\bar{x}, \bar{y}) = \bar{\mathbf{r}}_\perp$ and R_b are given by $\{\bar{\mathbf{r}}_\perp, R_b\} = \int d\xi d^2\mathbf{r}_\perp \{\mathbf{r}_\perp, |\mathbf{r}_\perp|\} N_e(\mathbf{r}_\perp, \xi) [\int d\xi d^2\mathbf{r}_\perp N_e(\mathbf{r}_\perp, \xi)]^{-1}$, where R_b is the mean bubble radius, ξ is the local position coordinate along the propagation direction in the PIC simulation's moving window, and the integration limits encompass the full volume of the leading wakefield bucket [32]. It is seen that the LP-induced bubble centroid dominantly oscillates along the laser polarization (y) direction, with negligible perturbation along x, while, for CP, the centroid follows a relatively tighter spiral. The centroid excursion is always significantly less for CP, with $|\bar{y}|_{\rm CP,max}/|\bar{y}|_{\rm LP,max} \lesssim 0.3$. In another view, Fig. 5(b) plots $\bar{x}/R_b$ and $\bar{y}/R_b$ vs time, showing the $\pi/2$ out-of-phase x and y oscillations induced by CP. The bubble centroid oscillation is caused by the slip of the laser pulse envelope with respect to the laser field oscillations [62,63]—the CEP slip—and manifests as a bubble modulation frequency $\Delta\omega_m/\omega_0 \sim (v_p - v_g)/c$, where ω_0 is the laser central frequency and v_p and v_g are the phase and group velocities, respectively, in the plasma. The CEP slip gives a bubble modulation period $T_{\rm bubb} = 2\pi/\Delta\omega_m \sim (N_{\rm cr}/N_e)T_{\rm laser}$, where $T_{\rm laser} = 2\pi/\omega_0$ is the laser period. The modulation period in Fig. 5(b) is $\omega_0 T_{\rm bubb} \sim 60$, giving $T_{\rm bubb} \sim 9.3 T_{\rm laser}$, in good agreement with the density used in the simulation, $N_{\rm cr}/N_{e,\rm peak} \sim 9.1$.

The more confined CP-induced spiral motion of the bubble centroid [Fig. 5(a)] is suggestive of a more symmetric accelerating structure compared to the LP case, where the bubble is driven primarily along one transverse axis. To see the effect of transverse bubble motion on bunch acceleration, we plot in Fig. 5(c) the average axial field $\langle E_z(0, 0, \xi)\rangle$ in the accelerating phase of the propagating bubble as a function of time, where the average is taken from maximal negative E_z to $E_z = 0$. The open circles denote the times in the bubble evolution after the onset of bunch injection and acceleration. The LP-induced bubble oscillations clearly result in significantly more $\langle E_z\rangle$ modulation, which is coupled to greater modulation in the bubble's focusing field $\mathbf{E}_\perp$ and affects the perpendicular bunch momentum $\mathbf{p}_\perp$. The top panels in Fig. 5(d) show electron bunch transverse profiles at $\omega_0 t = 2000$ ($z = 80$ μm) for energy >2 MeV; the bottom panels show corresponding x and y lineouts. For CP, the simulation shows a tight central feature surrounded by an electron ring, while the LP result shows a beam mainly elongated along the laser polarization direction (y), with significant spreading also along the orthogonal direction (x). The divergence angles $\Delta\theta_x$ and $\Delta\theta_y$ are determined from a sequence of beam snapshots, which give $\Delta\theta_{\rm div}^{\rm CP} = 9$ mrad and $\Delta\theta_{\rm div}^{\rm LP} > 60$ mrad calculated from $\Delta\theta_{\rm div} = [(\Delta\theta_x^2 + \Delta\theta_y^2)/2]^{1/2}$. These results are consistent with the experiment. We note that, for LP as opposed to CP, laser-driven electron loss from the simulation window renders $\Delta\theta_{\rm div}^{\rm LP}$ an underestimate. The associated movies of transverse beam evolution under CP and LP are shown in Ref. [32], where the ring beams in the CP case are seen to result from spiral motion of accelerated electrons. In general, we do not experimentally observe strong beam asymmetry along the LP polarization direction (left-right in the experimental electron beam and spectrum images) as might be intuited from the simulation in Fig. 5(a). Figure 5(d) shows that bunch electrons also experience significant bubble field perturbations orthogonal to the LP direction. In addition, the strong jet density gradient orthogonal to the LP direction may stretch the electron beam in that direction as the laser and trailing wakefield slightly refract.

One scenario for electron ring formation in Fig. 4(a) is shown in the particle tracking PIC simulation in Fig. 4(d), where density down-ramp-injected electrons in the second

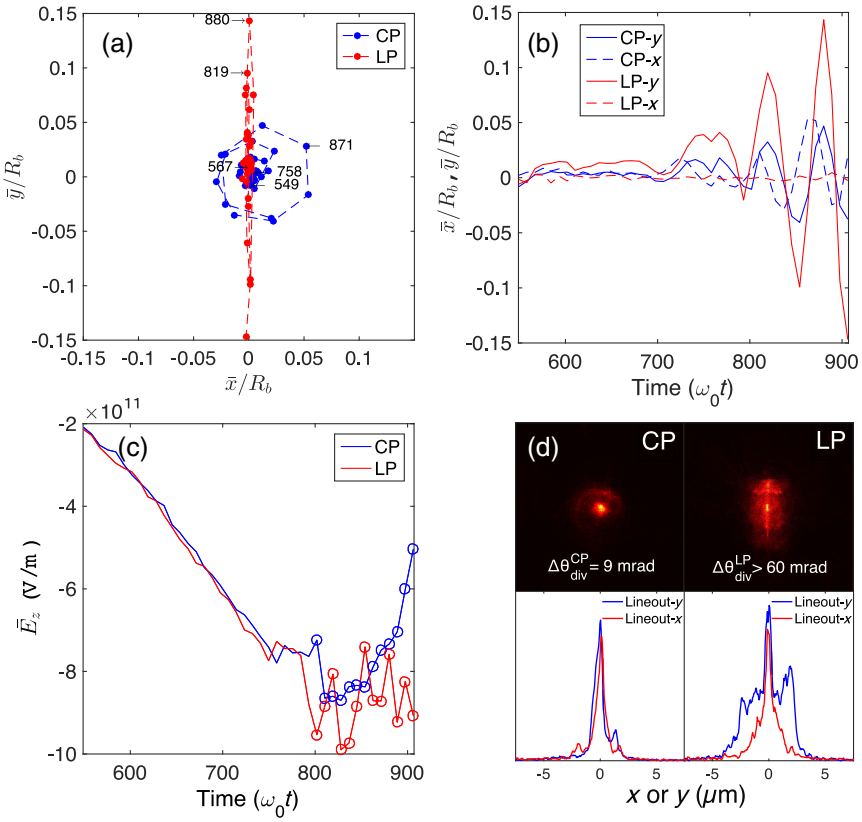

FIG. 5. Simulation parameters: LP or CP, 2.7 mJ, 5 fs, $\lambda_0 = 650$ nm, vacuum spot FWHM 4.5 μm, jet 140 μm FWHM, $N_e/N_{cr} = 0.11$, and center of neutral hydrogen jet placed at the beam waist ($z_{jet} = 0$). (a) Normalized bubble centroid position $(\bar{x}/R_b, \bar{y}/R_b)$ in transverse plane v. time. CP = circular polarization, LP = linear polarization. Numbers near points are values of $\omega_0 t$. (b)$\bar{x}/R_b$ and $\bar{y}/R_b$ vs time, showing the CEP slip-induced bubble centroid oscillations (see the text). (c) Average axial field $\langle E_z(0,0,\xi)\rangle$ in the accelerating phase of the bubble vs time for CP and LP pulses. The open circles are for times after electron injection and before bubble breakup. (d) Top: electron beam profiles (>2 MeV) at $\omega_0 t = 2000$ from CP and LP pulses, where the bunch is near $z = 80$ μm. The rms beam divergence $\Delta\theta_{div} = [(\Delta\theta_x^2 + \Delta\theta_y^2)/2]^{1/2}$ is shown in the panels. Bottom: beam lineouts along x and y. The LP direction is y (up-down).

bucket are driven in spiral orbits by the delayed and redshifted portion of the CP laser pulse, outrun the back of the first bucket, lose energy by dephasing, and are driven out transversely. The initial symmetry of the secondary bunch driven by CP is responsible for the ring shape, as seen on the right in Fig. 4(d). The electrons in the ring have a lower energy than those in the central spot (bottom left). For similar downramp focusing in the LP case in Fig. 3, electrons are also injected in the two leading buckets, but the second bucket electrons dephase and quickly diverge. We note that ringlike electron beams are reported in previous LWFA experiments and simulations under a range of different conditions using much longer duration circularly polarized laser pulses [64–67].

The strong reduction in electron beam divergence using few-cycle CP driver pulses is dramatically illustrated in Fig. 6, which compares results using CP and LP pulses focused at the jet center ($z_{jet} = 0$), where the highest energy electron bunches are expected. Electron beam profiles and energy spectra are shown for LP [Fig. 6(a)] and CP [Fig. 6(b)] for pulse energy 2.7 mJ and pulse width 5 fs. For CP, the electron beam energy is peaked at 15 MeV, with an intense central spot $\theta_{div} < 7$ mrad with <4 mrad shot-to-shot pointing jitter. This spot is superimposed on a wider ring-structured pedestal with the same energy, with divergence $\theta_{div} \sim 70$ mrad. By contrast, the electron beam divergence of $> \sim 200$ mrad for a LP driver is substantially larger. Lineouts of angle-integrated electron spectra are shown in Fig. 6(c), showing that the peak energies are similar for CP and LP, while the QME peak for CP is more distinct. Stability of the CP-driven beam is demonstrated by the spectra of ten consecutive shots (at 0.5 Hz) in Fig. 6(d). The total detected charge is similar in the two cases, approximately 2.5 pC. An important conclusion from these results is that a circularly polarized few-cycle LWFA driver pulse enables shot-to-shot stability of low-divergence, high-energy electron bunches without carrier-envelope phase stabilization.

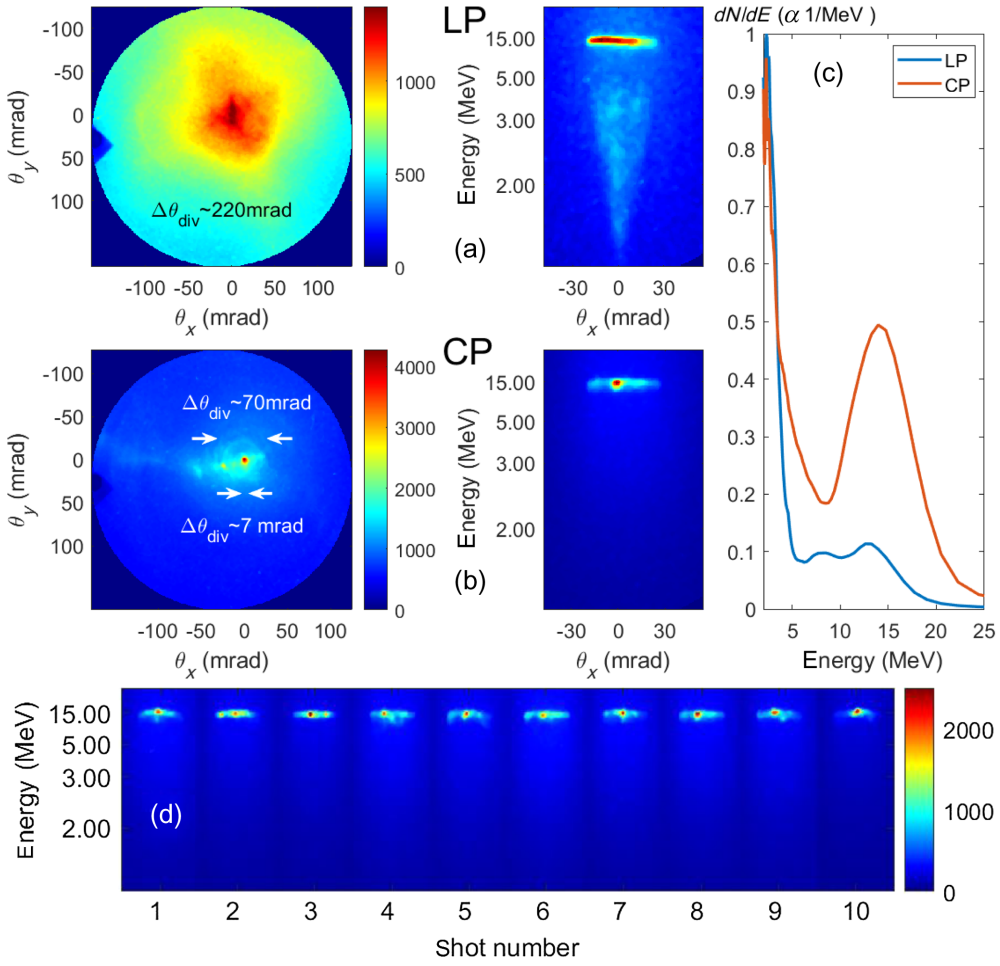

FIG. 6. Experimental conditions: 2.7-mJ, 5-fs LP or CP drive pulse, peak jet plasma density $N_{e,\mathrm{peak}}/N_{\mathrm{cr}} = 0.11$, $(P/P_{\mathrm{cr}})_{\mathrm{max}} \sim 3.4$, $z_{\mathrm{jet}} = 0$. (a) LP driver: electron beam profile (left) and corresponding energy spectrum (right). (b) CP driver: electron beam profile (left) and corresponding energy spectrum (right). The two values of $\Delta\theta_{\mathrm{div}}$ shown are for the central peak and the ringlike pedestal. (c) Electron spectrum lineouts on a linear scale for LP and CP drivers. Electron beam profiles and spectra are averaged over ten-shot bursts. (d) Electron spectra for ten consecutive CP shots at 0.5 Hz.

IV. CONCLUSIONS

The potential wide applicability of laser-plasma accelerators in the <20-MeV range has made use of high-repetition-rate, few-millijoule laser drivers an area of increasing interest. For such low-energy laser pulses to drive a relativistic plasma wave, strong relativistic self-focusing is needed, which requires operation at near-critical plasma densities $\sim 0.1 N_{\mathrm{cr}}$ and higher. For applications such as electron diffraction, where quasimonoenergetic electron bunches are desired, the plasma must be driven in the resonant bubble (or blowout) regime. At near-critical density, this requirement constrains the laser pulse to only a few optical cycles in duration, for which the difference in phase and group velocities in the dense plasma gives rise to significant CEP slip. Prior experiments and simulations using linearly polarized few-cycle driver pulses [27–29, 62,63] suggested that peak laser field modulations, induced by CEP slip, drive oscillations of the laser wakefield bubble, distorting the accelerating field experienced by an electron bunch and degrading its beam divergence. This effect is independent of whether or not the driver pulse is CEP stabilized.

Here, we have demonstrated record-high accelerated energy and low-divergence electron bunches using a near-critical-density hydrogen gas jet driven by few-millijoule, circularly polarized, few-cycle laser pulses which are not CEP stabilized. Specifically, circularly polarized, 5-fs, sub-3-mJ laser pulses generate pC-level, low-divergence (<10 mrad) electron bunches of energy up to 15 MeV from hydrogen jet plasmas of density $N_e/N_{\mathrm{cr}} \sim 0.1$. Linearly polarized drive pulses produce similar electron energy but more than an order of magnitude larger bunch divergence. Circular polarization mitigates the deleterious effects of

carrier-envelope phase slip, reducing bubble centroid oscillations and significantly improving beam divergence, while high electron beam energy is made possible by the more extended laser-plasma interaction length enabled by the hydrogen gas jet target. With a circularly polarized driver, the tighter, spiral motion of the wakefield bubble centroid leads to less perturbed plasma accelerating fields and significantly reduced sensitivity to shot-to-shot carrier-envelope phase variation. Reduced beam divergence is also achieved by focusing the few-cycle pulse in the plasma density downramp, where both CP and LP pulses drive milder wave breaking and reduced bubble oscillation, with CP pulses driving beams with approximately 3× less divergence than LP.

ACKNOWLEDGMENTS

The authors thank Luke Pascale for technical assistance. This research is supported by the U.S. Department of Energy (DESC0015516), the National Science Foundation (PHY2010511), and the Department of Homeland Security (2016DN077ARI104). M. K. is supported by the Air Force Office of Scientific Research (FA9550-18-1-0183).

[1] R. W. Hamm and M. E. Hamm, *The Beam Business: Accelerators in Industry*, Phys. Today **64**, No. 6, 46 (2011).

[2] A. W. Chao and W. Chou, *Medical Applications of Accelerators, Reviews of Accelerator Science and Technology Vol. 2* (World Scientific, Singapore, 2009).

[3] T. Tajima and J. M. Dawson, *Laser Electron Accelerator*, Phys. Rev. Lett. **43**, 267 (1979).

[4] E. Esarey, C. B. Schroeder, and W. P. Leemans, *Physics of Laser-Driven Plasma-Based Electron Accelerators*, Rev. Mod. Phys. **81**, 1229 (2009).

[5] F. Albert and A. G. R. Thomas, *Applications of Laser Wakefield Accelerator-Based Light Sources*, Plasma Phys. Controlled Fusion **58**, 103001 (2016).

[6] *Opportunities in Intense Ultrafast Lasers: Reaching for the Brightest Light* (The National Academies Press, Washington, DC, 2018), https://doi.org/10.17226/24939.

[7] B. Miao, L. Feder, J. E. Shrock, A. Goffin, and H. M. Milchberg, *Optical Guiding in Meter-Scale Plasma Waveguides*, Phys. Rev. Lett. **125**, 074801 (2020).

[8] C. Gahn, G. D. Tsakiris, G. Pretzler, K. J. Witte, P. Thirolf, D. Habs, C. Delfin, and C.-G. Wahlström, *Generation of MeV Electrons and Positrons with Femtosecond Pulses from a Table–Top Laser System*, Phys. Plasmas **9**, 987 (2002).

[9] A. Modena, Z. Najmudln, A. E. Dangor, C. E. Clayton, K. A. Marsh, C. Joshi, V. Malka, C. B. Darrow, C. Danson, D. Neely, and F. N. Walsh, *Electron Acceleration from the Breaking of Relativistic Plasma Waves*, Nature (London) **377**, 606 (1995).

[10] S. P. D. Mangles, C. D. Murphy, Z. Najmudin, A. G. R. Thomas, J. L. Collier, A. E. Dangor, E. J. Divall, P. S. Foster, J. G. Gallacher, C. J. Hooker, D. A. Jaroszynski, A. J. Langley, W. B. Mori, P. A. Norreys, F. S. Tsung, R. Viskup, B. R. Walton, and K. Krushelnick, *Monoenergetic Beams of Relativistic Electrons from Intense Laser–Plasma Interactions*, Nature (London) **431**, 535 (2004).

[11] C. G. R. Geddes, C. Toth, J. van Tilborg, E. Esarey, C. B. Schroeder, D. Bruhwiler, C. Nieter, J. Cary, W. P. Leemans, C. G. R. Geddes, C. Toth, J. van Tilborg, E. Esarey, C. B. Schroeder, D. Bruhwiler, C. Nieter, J. Cary, and W. P. Leemans, *High-Quality Electron Beams from a Laser Wakefield Accelerator Using Plasma-Channel Guiding*, Nature (London) **431**, 538 (2004).

[12] J. Faure, Y. Glinec, A. Pukhov, S. Kiselev, S. Gordienko, E. Lefebvre, J.-P. Rousseau, F. Burgy, and V. Malka, *A Laser–Plasma Accelerator Producing Monoenergetic Electron Beams*, Nature (London) **431**, 541 (2004).

[13] A. J. Gonsalves *et al.*, *Petawatt Laser Guiding and Electron Beam Acceleration to 8 GeV in a Laser-Heated Capillary Discharge Waveguide*, Phys. Rev. Lett. **122**, 084801 (2019).

[14] A. Picksley, A. Alejo, J. Cowley, N. Bourgeois, L. Corner, L. Feder, J. Holloway, H. Jones, J. Jonnerby, H. M. Milchberg, L. R. Reid, A. J. Ross, R. Walczak, and S. M. Hooker, *Guiding of High-Intensity Laser Pulses in 100-mm-Long Hydrodynamic Optical-Field-Ionized Plasma Channels*, Phys. Rev. Accel. Beams **23**, 081303 (2020).

[15] H. T. Kim, V. B. Pathak, K. Hong Pae, A. Lifschitz, F. Sylla, J. H. Shin, C. Hojbota, S. K. Lee, J. H. Sung, H. W. Lee, E. Guillaume, C. Thaury, K. Nakajima, J. Vieira, L. O. Silva, V. Malka, and C. H. Nam, *Stable Multi-GeV Electron Accelerator Driven by Waveform-Controlled PW Laser Pulses*, Sci. Rep. **7**, 10203 (2017).

[16] A. R. Maier, N. M. Delbos, T. Eichner, L. Hübner, S. Jalas, L. Jeppe, S. W. Jolly, M. Kirchen, V. Leroux, P. Messner, M. Schnepp, M. Trunk, P. A. Walker, C. Werle, and P. Winkler, *Decoding Sources of Energy Variability in a Laser-Plasma Accelerator*, Phys. Rev. X **10**, 031039 (2020).

[17] A. Döpp, E. Guillaume, C. Thaury, A. Lifschitz, F. Sylla, J. P. Goddet, A. Tafzi, G. Iaquanello, T. Lefrou, P. Rousseau, E. Conejero, C. Ruiz, K. Ta Phuoc, and V. Malka, *A Bremsstrahlung Gamma-Ray Source Based on Stable Ionization Injection of Electrons into a Laser Wakefield Accelerator*, Nucl. Instrum. Methods Phys. Res., Sect. A **830**, 515 (2016).

[18] G. C. Bussolino, A. Faenov, A. Giulietti, D. Giulietti, P. Koester, L. Labate, T. Levato, T. Pikuz, and L. A. Gizzi, *Electron Radiography Using a Table–Top Laser-Cluster Plasma Accelerator*, J. Phys. D **46**, 245501 (2013).

[19] S. P. D. Mangles, B. R. Walton, Z. Najmudin, A. E. Dangor, K. Krushelnick, V. Malka, M. Manclossi, N. Lopes, C. Carias, G. Mendes, and F. Dorchies, *Table–Top Laser-Plasma Acceleration as an Electron Radiography Source*, Laser Part. Beams **24**, 185 (2006).

[20] R. D. Edwards, M. A. Sinclair, T. J. Goldsack, K. Krushelnick, F. N. Beg, E. L. Clark, A. E. Dangor, Z. Najmudin, M. Tatarakis, B. Walton, M. Zepf, K. W. D. Ledingham, I. Spencer, P. A. Norreys, R. J. Clarke, R. Kodama, Y. Toyama, and M. Tampo, *Characterization of a Gamma-Ray Source Based on a Laser-Plasma Accelerator with Applications to Radiography*, Appl. Phys. Lett. **80**, 2129 (2002).

[21] Z. H. He, B. Beaurepaire, J. A. Nees, G. Gallé, S. A. Scott, J. R. S. Pérez, M. G. Lagally, K. Krushelnick, A. G. R.

Thomas, and J. Faure, *Capturing Structural Dynamics in Crystalline Silicon Using Chirped Electrons from a Laser Wakefield Accelerator*, Sci. Rep. **6**, 36224 (2016).

[22] J. Faure, B. Van Der Geer, B. Beaurepaire, G. Gallé, A. Vernier, and A. Lifschitz, *Concept of a Laser-Plasma-Based Electron Source for Sub-10-fs Electron Diffraction*, Phys. Rev. Accel. Beams **19**, 021302 (2016).

[23] A. G. Mordovanakis, J. Easter, N. Naumova, K. Popov, P. E. Masson-Laborde, B. Hou, I. Sokolov, G. Mourou, I. V. Glazyrin, W. Rozmus, V. Bychenkov, J. Nees, and K. Krushelnick, *Quasimonoenergetic Electron Beams with Relativistic Energies and Ultrashort Duration from Laser-Solid Interactions at 0.5 kHz*, Phys. Rev. Lett. **103**, 235001 (2009).

[24] S. Feister, D. R. Austin, J. T. Morrison, K. D. Frische, C. Orban, G. Ngirmang, A. Handler, J. R. H. Smith, M. Schillaci, J. A. LaVerne, E. A. Chowdhury, R. R. Freeman, and W. M. Roquemore, *Relativistic Electron Acceleration by MJ-Class KHz Lasers Normally Incident on Liquid Targets*, Opt. Express **25**, 18736 (2017).

[25] Z. H. He, B. Hou, J. A. Nees, J. H. Easter, J. Faure, K. Krushelnick, and A. G. R. Thomas, *High Repetition-Rate Wakefield Electron Source Generated by Few-Millijoule, 30 fs Laser Pulses on a Density Downramp*, New J. Phys. **15**, 053016 (2013).

[26] F. Salehi, A. J. Goers, G. A. Hine, L. Feder, D. Kuk, B. Miao, D. Woodbury, K. Y. Kim, and H. M. Milchberg, *MeV Electron Acceleration at 1 kHz with* <10 mJ *Laser Pulses*, Opt. Lett. **42**, 215 (2017).

[27] D. Guénot, D. Gustas, A. Vernier, B. Beaurepaire, F. Böhle, M. Bocoum, M. Lozano, A. Jullien, R. Lopez-Martens, A. Lifschitz, and J. Faure, *Relativistic Electron Beams Driven by KHz Single-Cycle Light Pulses*, Nat. Photonics **11**, 293 (2017).

[28] D. Gustas, D. Guénot, A. Vernier, S. Dutt, F. Böhle, R. Lopez-Martens, A. Lifschitz, and J. Faure, *High-Charge Relativistic Electron Bunches from a kHz Laser-Plasma Accelerator*, Phys. Rev. Accel. Beams **21**, 013401 (2018).

[29] L. Rovige, J. Huijts, I. Andriyash, A. Vernier, V. Tomkus, V. Girdauskas, G. Raciukaitis, J. Dudutis, V. Stankevic, P. Gecys, M. Ouille, Z. Cheng, R. Lopez-Martens, and J. Faure, *Demonstration of Stable Long-Term Operation of a Kilohertz Laser-Plasma Accelerator*, Phys. Rev. Accel. Beams **23**, 093401 (2020).

[30] A. Pukhov, J. Meyer-ter-vehn, and A. Physics, *Laser Wake Field Acceleration: The Highly Non-Linear Broken-Wave Regime*, Appl. Phys. B **74**, 355 (2002).

[31] W. Lu, M. Tzoufras, C. Joshi, F. S. Tsung, W. B. Mori, J. Vieira, R. A. Fonseca, and L. O. Silva, *Generating Multi-GeV Electron Bunches Using Single Stage Laser Wakefield Acceleration in a 3D Nonlinear Regime*, Phys. Rev. Accel. Beams **10**, 061301 (2007).

[32] See Supplemental Material at http://link.aps.org/supplemental/10.1103/PhysRevX.11.021055 (which includes Refs. [33–47]) for descriptions of few-cycle pulse generation and measurement, simulations of CP generation in the hollow core fiber, electron beam profile and energy spectrum measurement, fits to electron beam profiles, kappa distributions, and particle-in-cell simulations.

[33] A. Baltuska, M. Pshenichnikov, and D. Wiersma, *Second-Harmonic Generation Frequency-Resolved Optical Gating in the Single-Cycle Regime*, IEEE J. Quantum Electron. **35**, 459 (1999).

[34] R. Trebino, *Frequency-Resolved Optical Gating: the Measurement of Ultrashort Laser Pulses* (Kluwer Academic, Boston, 2000).

[35] M. Kolesik and J. V. Moloney, *Nonlinear Optical Pulse Propagation Simulation: From Maxwell's to Unidirectional Equations*, Phys. Rev. E **70**, 036604 (2004).

[36] A. Buck, K. Zeil, A. Popp, K. Schmid, A. Jochmann, S. D. Kraft, B. Hidding, T. Kudyakov, C. M. S. Sears, L. Veisz, S. Karsch, J. Pawelke, R. Sauerbrey, T. Cowan, F. Krausz, and U. Schramm, *Absolute Charge Calibration of Scintillating Screens for Relativistic Electron Detection*, Rev. Sci. Instrum. **81**, 033301 (2010).

[37] Y. Glinec, J. Faure, A. Guemnie-Tafo, V. Malka, H. Monard, J. P. Larbre, V. De Waele, J. L. Marignier, and M. Mostafavi, *Absolute Calibration for a Broad Range Single Shot Electron Spectrometer*, Rev. Sci. Instrum. **77**, 103301 (2006).

[38] J. C. Lagarias, J. A. Reeds, M. H. Wright, and P. E. Wright, *Convergence Properties of the Nelder-Mead Simplex Method in Low Dimensions*, SIAM J. Optim. **9**, 112 (1998).

[39] B. Beaurepaire, A. Lifschitz, and J. Faure, *Electron Acceleration in Sub-Relativistic Wakefields Driven by Few-Cycle Laser Pulses*, New J. Phys. **16**, 023023 (2014).

[40] S. Xu, J. Zhang, N. Tang, S. Wang, W. Lu, and Z. Li, *Periodic Self-Injection of Electrons in a Few-Cycle Laser Driven Oscillating Plasma Wake*, AIP Adv. **10**, 095310 (2020).

[41] G. Livadiotis, *Kappa Distributions: Theory and Applications in Plasmas* (Elsevier Science, New York, 2017).

[42] R. A. Treumann, C. H. Jaroschek, and M. Scholar, *Stationary Plasma States Far from Equilibrium*, Phys. Plasmas **11**, 1317 (2004).

[43] R. A. Treumann and C. H. Jaroschek, *Gibbsian Theory of Power-Law Distributions*, Phys. Rev. Lett. **100**, 155005 (2008).

[44] M. A. Hellberg, R. L. MacE, T. K. Baluku, I. Kourakis, and N. S. Saini, *Comment on "Mathematical and Physical Aspects of Kappa Velocity Distribution,"* Phys. Plasmas **14**, 110702 (2007)]; Phys. Plasmas **16**, 094701 (2009).

[45] L. N. Hau and W. Z. Fu, *Mathematical and Physical Aspects of Kappa Velocity Distribution*, Phys. Plasmas **14**, 110702 (2007).

[46] A. Hasegawa, K. Mima, and M. Duong-Van, *Plasma Distribution Function in a Superthermal Radiation Field*, Phys. Rev. Lett. **54**, 2608 (1985).

[47] T. D. Arber, K. Bennett, C. S. Brady, A. Lawrence-Douglas, M. G. Ramsay, N. J. Sircombe, P. Gillies, R. G. Evans, H. Schmitz, A. R. Bell, and C. P. Ridgers, *Contemporary Particle-in-Cell Approach to Laser-Plasma Modelling*, Plasma Phys. Controlled Fusion **57**, 113001 (2015).

[48] F. Böhle, M. Kretschmar, A. Jullien, M. Kovacs, M. Miranda, R. Romero, H. Crespo, U. Morgner, P. Simon, R. Lopez-Martens, and T. Nagy, *Compression of CEP-Stable Multi-mJ Laser Pulses down to 4 fs in Long Hollow Fibers*, Laser Phys. Lett. **11**, 095401 (2014).

[49] F. Salehi, *High Repetition Rate Laser-Driven Electron Acceleration to Mega-Electron-Volt Energies*, University of Maryland College Park, 2019 (https://drum.lib.umd.edu/handle/1903/25043).

[50] F. Salehi, A. J. Goers, L. Feder, B. Miao, D. Woodbury, and H. M. Milchberg, *Characterization of a 100 Micrometer-Scale Cryogenically Cooled Gas Jet for Near-Critical Density Laser-Plasma Experiments*, Rev. Sci. Instrum. **90**, 103001 (2019).

[51] A. J. Goers, G. A. Hine, L. Feder, B. Miao, F. Salehi, J. K. Wahlstrand, and H. M. Milchberg, *Multi-MeV Electron Acceleration by Subterawatt Laser Pulses*, Phys. Rev. Lett. **115**, 194802 (2015).

[52] D. Woodbury, L. Feder, V. Shumakova, C. Gollner, R. Schwartz, B. Miao, F. Salehi, A. Korolov, A. Pugžlys, A. Baltuška, and H. M. Milchberg, *Laser Wakefield Acceleration with Mid-IR Laser Pulses*, Opt. Lett. **43**, 1131 (2018).

[53] P. B. Corkum, C. Rolland, and T. Srinivasan-Rao, *Supercontinuum Generation in Gases*, Phys. Rev. Lett. **57**, 2268 (1986).

[54] X. Chen, A. Jullien, A. Malvache, L. Canova, A. Borot, and A. Trisorio, *C. G. Durfee, and R. Lopez-Martens, Generation of 4.3 fs, 1 mJ Laser Pulses via Compression of Circularly Polarized Pulses in a Gas-Filled Hollow-Core Fiber*, Opt. Lett. **34**, 1588 (2009).

[55] L. Railing, M. Le, F. Salehi, M. Kolesik, and H. M. Milchberg, *Polarization Effect on Bandwidth Broadening in Hollow Core Fibers* (to be published).

[56] M. Kolesik, J. V. Moloney, and E. M. Wright, *Polarization Dynamics of Femtosecond Pulses Propagating in Air*, Phys. Rev. E **64**, 046607 (2001).

[57] P. Sprangle, C. M. Tang, and E. Esarey, *Relativistic Self-Focusing of Short-Pulse Radiation Beams in Plasmas*, IEEE Trans. Plasma Sci. **15**, 145 (1987).

[58] S. Bulanov, N. Naumova, F. Pegoraro, and J. Sakai, *Particle Injection into the Wave Acceleration Phase due to Nonlinear Wake Wave Breaking*, Phys. Rev. E **58**, R5257 (1998).

[59] C. G. R. Geddes, K. Nakamura, G. R. Plateau, C. Toth, E. Cormier-Michel, E. Esarey, C. B. Schroeder, J. R. Cary, and W. P. Leemans, *Plasma Density Gradient Injection of Low Absolute Momentum Spread Electron Bunches*, Phys. Rev. Lett. **100**, 215004 (2008).

[60] C. M. S. Sears, A. Buck, K. Schmid, J. Mikhailova, F. Krausz, and L. Veisz, *Emittance and Divergence of Laser Wakefield Accelerated Electrons*, Phys. Rev. Accel. Beams **13**, 092803 (2010).

[61] R. Weingartner, S. Raith, A. Popp, S. Chou, J. Wenz, K. Khrennikov, M. Heigoldt, A. R. Maier, N. Kajumba, M. Fuchs, B. Zeitler, F. Krausz, S. Karsch, and F. Grüner, *Ultralow Emittance Electron Beams from a Laser-Wakefield Accelerator*, Phys. Rev. ST Accel. Beams **15**, 111302 (2012).

[62] E. N. Nerush and I. Y. Kostyukov, *Carrier-Envelope Phase Effects in Plasma-Based Electron Acceleration with Few-Cycle Laser Pulses*, Phys. Rev. Lett. **103**, 035001 (2009).

[63] J. Huijts, I. Andriyash, L. Rovige, A. Vernier, and J. Faure, *Identifying Observable Carrier-Envelope Phase Effects in Laser Wakefield Acceleration with Near-Single-Cycle Pulses*, Phys. Plasmas **28**, 043101 (2021).

[64] A. Sharma, *High Energy Electron and Proton Acceleration by Circularly Polarized Laser Pulse from Near Critical Density Hydrogen Gas Target*, Sci. Rep. **8**, 2191 (2018).

[65] B. Gonzalez-Izquierdo, M. King, R. J. Gray, R. Wilson, R. J. Dance, H. Powell, D. A. MacLellan, J. McCreadie, N. M. H. Butler, S. Hawkes, J. S. Green, C. D. Murphy, L. C. Stockhausen, D. C. Carroll, N. Booth, G. G. Scott, M. Borghesi, D. Neely, and P. McKenna, *Towards Optical Polarization Control of Laser-Driven Proton Acceleration in Foils Undergoing Relativistic Transparency*, Nat. Commun. **7**, 12891 (2016).

[66] Y. Ma, D. Seipt, A. E. Hussein, S. Hakimi, N. F. Beier, S. B. Hansen, J. Hinojosa, A. Maksimchuk, J. Nees, K. Krushelnick, A. G. R. Thomas, and F. Dollar, *Polarization-Dependent Self-Injection by Above Threshold Ionization Heating in a Laser Wakefield Accelerator*, Phys. Rev. Lett. **124**, 114801 (2020).

[67] B. B. Pollock, F. S. Tsung, F. Albert, J. L. Shaw, C. E. Clayton, A. Davidson, N. Lemos, K. A. Marsh, A. Pak, J. E. Ralph, W. B. Mori, and C. Joshi, *Formation of Ultrarelativistic Electron Rings from a Laser-Wakefield Accelerator*, Phys. Rev. Lett. **115**, 055004 (2015).